Designed Synthesis of CeO_2 Nanorods and Nanowires for Studying Toxicological Effects of High Aspect Ratio Nanomaterials

Zhaoxia Ji,[†] Xiang Wang,[†] Haiyuan Zhang,[†] Sijie Lin,[†] Huan Meng,[‡] Bingbing Sun,[‡] Saji George,[†,‡] Tian Xia,[†,‡] André E. Nel,[†,‡] and Jeffrey I. Zink[†,§,*]

[†]Center for Environmental Implications of Nanotechnology, California NanoSystems Institute, [‡]Department of Medicine, Division of NanoMedicine, and [§]Department of Chemistry and Biochemistry, University of California at Los Angeles, Los Angeles, California 90095, United States

ABSTRACT

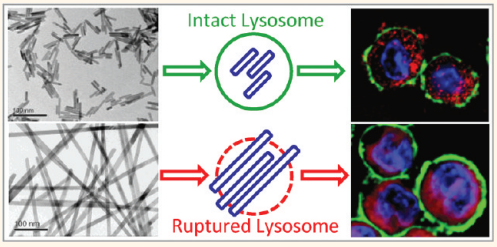

While it has been shown that high aspect ratio nanomaterials like carbon nanotubes and TiO_2 nanowires can induce toxicity by acting as fiber-like substances that damage the lysosome, it is not clear what the critical lengths and aspect ratios are that induce this type of toxicity. To answer this question, we synthesized a series of cerium oxide (CeO_2) nanorods and nanowires with precisely controlled lengths and aspect ratios. Both phosphate and chloride ions were shown to play critical roles in obtaining these high aspect ratio nanostructures. High-resolution TEM analysis shows that single-crystalline CeO_2 nanorods/nanowires were formed along the [211] direction by an "oriented attachment" mechanism, followed by Ostwald ripening. The successful creation of a comprehensive CeO_2 nanorod/nanowire combinatorial library allows, for the first time, the systematic study of the effect of aspect ratio on lysosomal damage, cytotoxicity, and IL-1β production by the human myeloid cell line (THP-1). This *in vitro* toxicity study demonstrated that, at lengths $\geq$200 nm and aspect ratios $\geq$22, CeO_2 nanorods induced progressive pro-inflammatory effects and cytotoxicity. The relatively low "critical" length and aspect ratio were associated with small nanorod/nanowire diameters (6–10 nm), which facilitates the formation of stacking bundles due to strong van der Waals and dipole–dipole attractions. Our results suggest that both length and diameter components of aspect ratio should be considered when addressing the cytotoxic effects of high aspect ratio materials.

KEYWORDS: cerium oxide · nanorods · nanowires · aspect ratio · hydrothermal synthesis · oriented attachment · Ostwald ripening · frustrated phagocytosis

High aspect ratio nanomaterials, such as nanorods, nanotubes, and nanowires, have attracted widespread attention due to their unique chemical, mechanical, electric, and optical properties and their promising applications in nanodevices.[1−5] Despite the increasing interest in production and use of these materials, concerns have been raised about their potential adverse health and environmental effects. Many studies show that both the length as well as aspect ratio of nanorods and nanowires play significant roles in their biological reactivity.[6−8] Above a length of 15 μm, some high aspect ratio materials such as asbestos fibers fail to be engulfed by macrophages, leading to frustrated phagocytosis and chronic granulomatous inflammation.[7,9,10] Another type of bioreactivity is activation of the NALP3 inflammasome and IL-1β production, which has been shown to play a role in the generation of chronic granulomatous inflammation and fibrosis by multiwalled carbon nanotubes.[11,12] Although other material types may also fit the "fiber paradigm",[13−15] these studies only explored a very limited number of lengths and aspect ratios (typically from one to three), thereby failing to clarify the threshold above which length and aspect ratio engage the lysosomal pathway that leads to inflammasome activation. To address this issue, a library of nanomaterials with the same chemical composition but a wide range of aspect ratios is required. For this reason, we created a cerium oxide (CeO_2) nanorod/nanowire library with finely tuned aspect ratios. The advantage of using CeO_2 is that this material is frequently inert at biological level or may even act as an antioxidant;[16−19] this allows an appropriate comparison of its change in toxicity upon the change in its length and aspect ratio. The fact that some commercial products do include CeO_2 nanorods and nanowires as unintended components makes it more imperative to assess the safety of high aspect ratio CeO_2 nanomaterials and understand their behavior in biological systems.

Various methods including sol–gel,[20,21] precipitation,[22] hydrothermal,[23−28] and thermal decomposition[29] have been reported

* Address correspondence to zink@chem.ucla.edu.

Received for review March 19, 2012 and accepted May 7, 2012.

Published online May 07, 2012
10.1021/nn3012114

for preparing one-dimensional (1-D) CeO_2 nanorods, nanowires, or nanotubes. Among these reported approaches, hydrothermal synthesis has been most extensively investigated because it is a simple and cost-effective method. Very often, a variety of chemical reagents, surfactants, or organic templates have to be introduced during hydrothermal synthesis to direct the anisotropic growth of CeO_2 nanocrystals.[26,27,30−32] It should be noted that the use of chemical additives and the successive removal process may contaminate CeO_2 nanorods and influence the potential applications or biological responses and therefore should be avoided if possible. Synthesis of 1-D CeO_2 nanostructures in the absence of any organic templates or surfactants is desirable, even though it is more difficult to achieve. The most commonly used strategy to prepare 1-D CeO_2 nanostructures in a template-free system is to introduce precursors or intermediate species of anisotropic structures so that 1-D CeO_2 can be formed *via* topotactic inheritance of those structures. Typically a Ce^{3+} salt [$CeCl_3$ or $Ce(NO_3)_3$] is mixed with a high concentration alkaline solution, leading to the formation of $Ce(OH)_3$ nanorod nuclei. After drying, these rod-like $Ce(OH)_3$ nanocrystals can be converted to CeO_2 without any shape changes.[22,28,33,34] The $Ce(OH)_3$ nanorods can also be transformed into CeO_2 nanotubes if they are treated with a H_2O_2 solution under ultrasonic conditions.[35] In spite of the effectiveness of this method, precise control of CeO_2 particle size and shape still remains a big challenge. Because $Ce(OH)_3$ is unstable and extremely sensitive to oxygen, it can be easily oxidized by NO_3^- or dissolved oxygen during the precipitation process, leading to the formation of CeO_2 nanocubes. That is why very often only a part of the CeO_2 product maintained a nanorod morphology.[25,28] In addition, nanoparticles obtained from a highly alkaline system usually are severely agglomerated/aggregated and cannot be easily redispersed, which is not surprising considering the fact that the $Ce(OH)_3$ precipitate is the actual precursor of CeO_2 nanoparticles. To obtain better dispersed CeO_2 nanoparticles with a narrow size distribution, synthesis in an acidic medium would be preferred.[36] Although it is much more challenging, Xing and co-workers[23,24] demonstrated that, by using a very small amount of Na_3PO_4 as a mineralizer, it is still possible to obtain CeO_2 nanorods under acidic conditions. The authors did not attempt to finely tune the aspect ratio of these nanorods mainly because the nanorods could only form in a very narrow synthesis window and a slight change in synthesis composition and condition led to a totally different nanostructure.[24]

In this investigation, we demonstrate an effective surfactant and organic template-free hydrothermal technique for preparing high-purity and high-crystallinity CeO_2 nanorods and nanowires. By controlling synthesis compositions and conditions, lengths and aspect ratios of these CeO_2 nanorods and nanowires can be precisely controlled and finely tuned over a wide range. The CeO_2 nanorods obtained from the primary synthesis can also be reconstructed into even longer nanorods/nanowires by additional hydrothermal treatment. Efforts have also been made to understand the crystallization mechanism of CeO_2 nanorods and nanowires in both primary and secondary synthesis systems. The successful creation of this broad CeO_2 nanorod/nanowire combinatorial library allows, for the first time, the systematic study of pure length and aspect ratio effect on biological activity of this material. The human monomyelocytic leukemia cell line, THP-1, was selected as the cellular model to study the impact of high aspect ratio CeO_2 nanorods/nanowires on the activation of the NALP3 inflammasome, which has been demonstrated to play a role in the generation of pulmonary inflammation and fibrosis during exposure to asbestos fibers and multiwalled carbon nanotubes.[37,38] This inflammasome is activated as a result of lysosomal damage by high aspect ratio materials in phagocytic cells. THP-1 cells are used experimentally to simulate the sequence of events that take place during the generation of "frustrated phagocytosis" by asbestos fibers in the lung.[37]

RESULTS AND DISCUSSION

Shape and Aspect Ratio Control of CeO_2 Nanorods. In a typical hydrothermal synthesis system, formation of nanoparticles starts with nucleation from the precursor solution followed by growth of the resulting nuclei. By varying synthesis compositions and conditions, both the shape of nuclei and the growth direction of the nuclei can be manipulated to obtain nanoparticles with desired morphology in the final product. On the basis of this knowledge, selected variables that have been identified as key in controlling nucleation and crystal growth were explored in this investigation. These include (i) cerium precursor type and concentration; (ii) concentration of phosphate; (iii) reaction temperature; (iv) pH of the synthesis mixture; and (v) seeding and secondary treatment. By varying the synthesis conditions and compositions, CeO_2 nanorods/nanowires with precisely controlled aspect ratios can be obtained.

Effect of Cerium Precursors. The type of cerium salt and the concentration directly influence the size and morphology of CeO_2 nanoparticles. In this study, four different cerium sources including cerium(III) sulfate ($Ce_2(SO_4)_3$), cerium(IV) sulfate ($Ce(SO_4)_2$), cerium(III) nitrate ($Ce(NO_3)_3$), and cerium(III) chloride ($CeCl_3$) were explored. Only when $CeCl_3$ was used as the cerium precursor were pure nanorods obtained using a wide range of synthesis compositions and conditions. The observed cerium source effect involves the combined effects of cerium ions (Ce^{3+} *vs* Ce^{4+}) as well as associated counteranions (SO_4^{2-}, NO_3^-, and Cl^-). When Ce

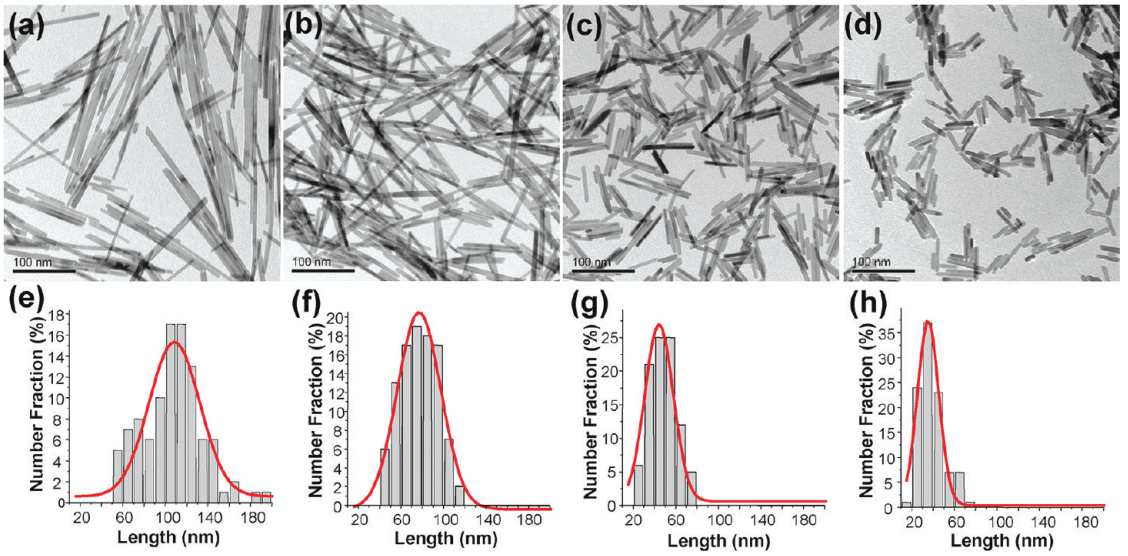

Figure 1. TEM images (a–d) and length distribution analysis (e–h) of CeO_2 nanorods obtained after 15 h hydrothermal treatment at 220 °C with different initial $CeCl_3$ concentrations: (a,e) 0.025 M; (b,f) 0.05 M; (c,g) 0.10 M; (d,h) 0.20 M.

in the +3 oxidation state is used, an oxidation step converting Ce^{3+} into Ce^{4+} becomes necessary. Because of this additional step, the nucleation and crystal growth and thus nanoparticle size and morphology are very different from those in the synthesis using a Ce^{4+} salt.[22,28,39] The counteranions in cerium salts can also play an important role in controlling the size and morphology of CeO_2 nanoparticles. Wu *et al.*[25] demonstrated that anions including Cl^-, Br^-, and I^- promoted the formation of nanorods, whereas NO_3^- favored the synthesis of nanocubes. It was suggested that halide anions could adsorb onto the surfaces of the initial $Ce(OH)_3$ nanorod nuclei, therefore stabilizing the rod shape. In contrast, the presence of oxidizing anions like NO_3^- could gradually convert the nanorods into nanocubes. A similar structure-stabilizing role of Cl^- ions was reported by Wang *et al.* in their CeO_2 nanowire synthesis system.[40] Although these findings may not be generalized to all CeO_2 hydrothermal systems, they clearly showed the importance of the cerium source in controlling CeO_2 nanoparticle size and shape.

Figure 1a–d shows the CeO_2 nanorods obtained with the $CeCl_3$ concentration varying from 0.025 to 0.20 M while keeping other synthesis composition and conditions constant. All samples were composed of fairly uniform single-crystalline nanorods. X-ray diffraction analysis showed that cubic fluorite CeO_2 (JCPDS 34-0394, space group *Fm*3*m*) was the only phase present in the final products (Figure S1 in Supporting Information). The rods clearly became shorter with increasing $CeCl_3$ concentrations while remaining relatively constant in diameter. The size measurement based on TEM images also confirmed a very narrow length distribution of the rods (Figure 1e–h). More detailed information on nanorod dimensions and the corresponding aspect ratio (*R*) are listed in Table 1,

TABLE 1. Effects of $CeCl_3$ Concentration, Initial pH, and Synthesis Temperature on CeO_2 Nanorod Length (*L*), Diameter (*D*), and Corresponding Aspect Ratio (*R*)

experiment #	C_{CeCl_3} (mol L^{-1})	pH	*T* (°C)	*L* (nm)	*D* (nm)	*R*
1	0.025	4.2	220	106.7	6.6	16.2
2	0.05	4.1	220	76.8	6.5	11.8
3	0.1	4.0	220	50.8	6.7	7.6
4	0.2	4.0	220	38.8	6.8	5.7
5	0.4	3.5	220	33.2	8.0	4.2
6	0.6	3.4	220	31.5	7.7	4.1
7	0.1	4.0	140	77.5	6.2	12.5
8	0.1	4.0	170	58.9	7.1	8.3
9	0.1	4.0	240	42.1	6.8	6.2

which shows a gradual decrease in the average length of CeO_2 nanorods with increasing $CeCl_3$ concentrations. As a result, the aspect ratio of these nanorods was systematically tuned from 4.1 to 16.2, simply by adjusting the $CeCl_3$ concentration from 0.60 to 0.025 M. The relatively constant diameter for all nanorods suggests that the growth is limited in the transverse direction. On the other hand, the different growth rate in the longitudinal direction could be attributed to the change of supersaturation level with $CeCl_3$ concentration. According to the classical crystallization mechanism, nucleation and crystal growth rates are determined by the supersaturation level of the synthesis system.[41] At low supersaturation, crystals grow faster than they nucleate, therefore resulting in larger crystals. In contrast, at higher supersaturation, nucleation dominates crystal growth, ultimately leading to the formation of a larger number of smaller particles. Because the lateral growth of the nanorods is confined in the current system, the supersaturation could effectively affect the growth in the longitudinal direction and thus the nanorod length. A higher $CeCl_3$

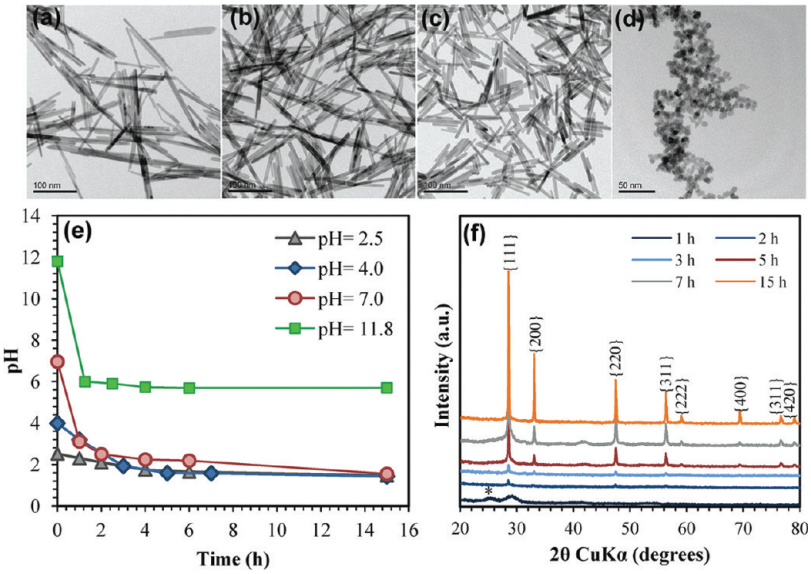

Figure 2. TEM images of CeO_2 nanorods obtained from a synthesis mixture with 0.1 M $CeCl_3$ and pH of (a) 1.8, (b) 2.5, (c) 4.0, (d) 11.8; (e) pH evolution as a function of time during the course of crystallization; (f) XRD patterns of CeO_2 nanorods obtained from the synthesis with initial pH of 4.0 after hydrothermal treatment for 1, 2, 3, 5, 7, and 15 h. The asterisk * indicates the reflection due to $CePO_4$. All syntheses were conducted at 220 °C.

concentration that corresponds to higher supersaturation levels will result in faster nucleation and thus a larger number of shorter CeO_2 nanorods. When the $CeCl_3$ concentration was increased to 0.4 M, the supersaturation seems to reach an extremely high level; therefore, no significant change in nanorod length was observed beyond this concentration (Table 1).

Effect of Reaction Temperature. Temperature also had an impact on the aspect ratio of CeO_2 nanorods. Over a temperature range of 140−240 °C, all particles assumed a rod-like morphology. The nanorods became shorter and thus had lower aspect ratios with increasing reaction temperature (Table 1, experiments 7−9). The observed length and aspect ratio change reflected a temperature effect on the CeO_2 crystallization process. Because a higher temperature resulted in faster nucleation, a larger number of small nuclei were formed. For a given amount of synthesis precursor, shorter CeO_2 nanorods were formed at higher temperatures. At all synthesis temperatures, the nanorods appeared to be very stable, even after long (72 h) hydrothermal treatment. These results are very different from those reported in the literature, where often CeO_2 nanorods can be synthesized at a relatively low temperature (≤100 °C) only.[22,28] In some cases, different morphologies could be obtained at the same temperature or *vice versa*, all depending on the hydrothermal treatment time and synthesis mixture composition, which makes the temperature effect very complicated.[23,24] We believe that the difference between the present study and others reported in the literature is due to the different synthesis compositions and conditions used in each system. It is the unique combination of Cl^- and phosphate ions in our system that allows the formation of highly crystalline, stable CeO_2 nanorods at different synthesis temperatures.

Role of Phosphate Ions. The presence of phosphate ions is key in preparing CeO_2 nanorods in the current system, without which only large octahedra were obtained. Typically 1×10^{-3} M of Na_3PO_4 was sufficient for producing pure nanorods, but when the phosphate concentration was raised above 1×10^{-2} M, cerium phosphate ($CePO_4$) impurities started to appear in the product, as confirmed by XRD analysis (data not shown). Within the 1×10^{-3} to 1×10^{-2} M concentration range, CeO_2 nanorod formation did not show any significant dependence on the phosphate concentration. Therefore, the phosphate concentration was kept at 5×10^{-3} M unless otherwise mentioned. It should be noted that the mediation effect of phosphate ions was only observed under acidic conditions. At an alkaline pH, only CeO_2 nanocubes were obtained regardless of whether Na_3PO_4 was used.

Effect of Synthesis pH. Experiments with pH varying from 2 to 12 confirmed that CeO_2 nanorods only formed under acidic conditions, and within the acidic pH range, the nanorods grew longer at a lower pH (Figure 2a−c). However, when the synthesis pH was raised above 10, only nanocubes were obtained (Figure 2d, pH 11.8). CeO_2 nanorods obtained at a low pH (~2.0) but with the same synthesis composition as those for nanorods shown in Figure 1a,c,d are presented in Figure S2a−c, respectively. It is clear that all nanorods synthesized at pH 2.0 are much longer than those obtained at the natural synthesis pH (4.0−4.2, without any pH adjustment). Consistent with what was demonstrated earlier, a lower $CeCl_3$ concentration always resulted in longer nanorods, with the

lowest $CeCl_3$ concentration of 0.025 M resulting in a product with a nanowire-like morphology and length >1 μm (Figure S2a). To understand in more detail the effect of pH on CeO_2 nucleation and crystallization, the evolution of pH with reaction time was monitored. Figure 2e shows four syntheses conducted at 220 °C with the same $CeCl_3$ concentration (0.1 M) but different initial pH values. For each synthesis, six autoclaves were used and one autoclave was removed from the electric oven at each desired time interval. The reaction was quenched rapidly by cooling the autoclaves in cold water, and the pH of the reaction solution was then measured. In all cases, a sharp drop in pH was observed within the first 1−2 h. As the reaction proceeded, the pH changed more slowly and completely stopped after 5 h even though all reactions were extended to 15 h. On the other hand, XRD analysis revealed the rapid crystallinity increase in the first several hours followed by much slower change at the later stage (Figure 2f). The extent of CeO_2 crystallization correlates with the evolution of the pH during the course of the synthesis. The initial sharp decrease in pH suggests a large consumption of hydroxyl ions during nucleation and the Ce^{3+} oxidation step. The constant pH at the later stage implies that Ostwald ripening dominated during the crystal growth stage, involving both the dissolution and recrystallization of nanoparticles.

Reconstruction of CeO_2 Nanorods/Nanowires by Secondary Hydrothermal Treatment. Although the length and aspect ratio of CeO_2 nanorods could be systematically tuned by controlling the synthesis composition and conditions, nanorods were usually shorter than 100 nm. Only the synthesis with pH 2.0 and the lowest $CeCl_3$ concentration (0.025 M) yielded relatively long CeO_2 nanowires. However, the yield was relatively low in this case. Therefore, synthesis of high aspect ratio CeO_2 nanorods/nanowires with high yield during primary synthesis remains quite challenging. As an alternative method, secondary hydrothermal treatment including a multistep seeded growth approach was explored. It has been shown in many studies that the secondary growth method could be a very effective route for preparing nanostructured materials covering a large size or shape range.[42−44] A typical seeding experiment consists of two steps, where crystals grown in the first step using a standard synthesis mixture are used as seeds in the second step. In principle, the added seeds can continue to grow in the second step with new crystals forming from primary nucleation simultaneously. However, at a high seeding concentration, the depletion of the precursor due to seed crystal growth may stop the primary nucleation and thus eliminate the formation of new crystals. Under this condition, seed crystals will grow into larger particles and the final particle size can be controlled by adjusting the seeding concentration. In this investigation, both CeO_2 seeding concentrations and synthesis mixture compositions were explored in an attempt to grow longer nanorods/nanowires.

Our first goal was to find an optimum seeding concentration, for which experiments with a series of seeding levels (*i.e.*, 0.1, 1.0, 10.0 wt.%) were performed (these seeding levels were calculated based on the mass of the CeO_2 product obtained from a standard synthesis). Surprisingly, at all seeding levels, no noticeable difference in size or shape was observed between the nanorods obtained from the seeding experiments and the seed crystals (Figure S3). These results suggest little or no growth of the seed crystals in the secondary growth experiments. In other words, most, if not all, of the nanorods in the final products should be newly formed crystals as a result of primary nucleation. To eliminate the potential primary nucleation, $CeCl_3$ as the cerium precursor was completely removed from the secondary treatment system and only a 5×10^{-3} M Na_3PO_4 aqueous solution was used. Both pH and the type of acid used for pH adjustment were explored in this secondary treatment step.

No noticeable change in size and shape of the final product was observed when the secondary treatment was conducted at pH 4.0 (this pH was initially selected to match that for the standard synthesis mixture). However, when the pH was lowered to ~2.0 using hydrochloric acid, the CeO_2 nanorods were successfully reconstructed into longer nanorods and nanowires, and the aspect ratio could be finely tuned by selecting the type of seeds and seeding levels. For example, when the nanorods obtained from experiment 3 in Table 1 ($L \times D = 50.8$ nm $\times$ 6.7 nm, Figure 3a) were added into the secondary treatment aqueous solution, they were converted into nanowires with dimensions of 1.0−1.5 μm $\times$ 11.2 nm (Figure 3d). Similarly, using the seeds with dimensions 38.8 nm $\times$ 6.8 nm (Figure 3b) and 33.2 nm $\times$ 8.0 nm (Figure 3c) yielded nanorods with dimensions of 173 nm $\times$ 8.7 nm (Figure 3e) and 77 nm $\times$ 10.3 nm (Figure 3f), respectively. Since there is no cerium source present in the secondary treatment system, the longer nanorods/nanowires must have been directly reconstructed from the seed nanorods through a "dissolution−recrystallization" mechanism. This was also supported by our crystallization kinetic experiment (Figure S4), which showed a gradual growth of nanorods upon the secondary hydrothermal treatment. Considering the critical roles that both Cl^- and phosphate ions played in the primary hydrothermal synthesis, it is not surprising to find out that both anions also were required in the secondary treatment process for producing pure CeO_2 nanorods/nanowires. When sodium phosphate was removed from the system, only a slight increase in CeO_2 nanorod length was observed. Very likely, the strong coordination of phosphate with cerium ions was the driving force for the nanorod "dissolution" under highly acidic

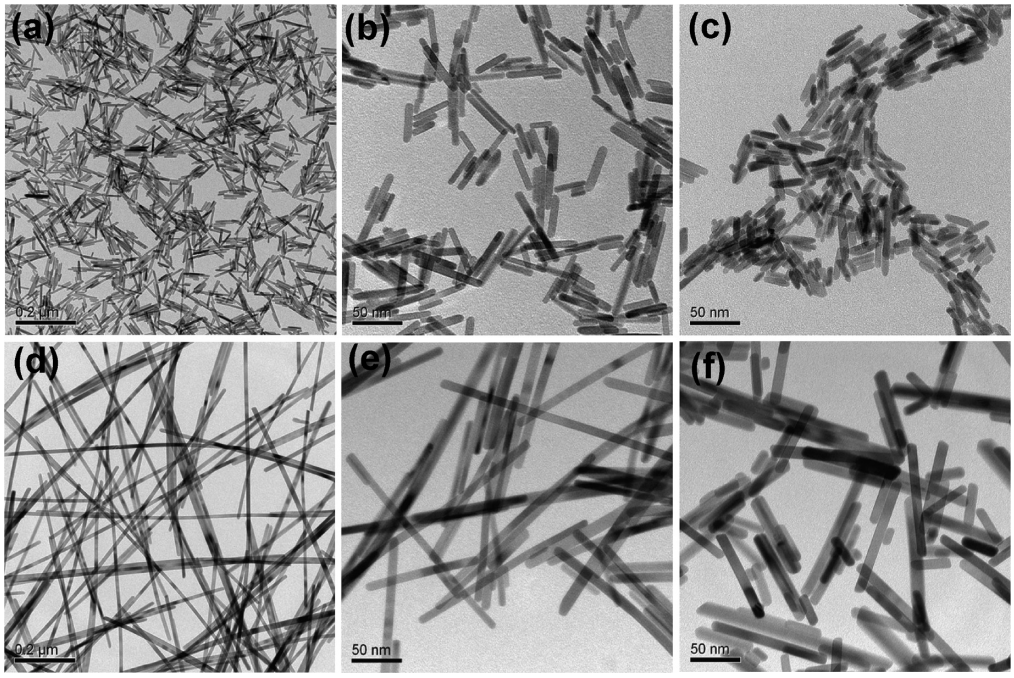

Figure 3. TEM analyses of CeO_2 nanorods obtained from (a−c) primary and (d−f) secondary synthesis. When CeO_2 nanorods obtained from primary synthesis, using (a) 0.1 M, (b) 0.2 M, and (c) 0.4 M $CeCl_3$, were used as seed crystals in a secondary hydrothermal treatment, CeO_2 nanowires or nanorods as shown in panels d, e, and f, were obtained. Both primary and secondary syntheses were conducted at 220 °C.

condition. The "coordination-assisted" dissolution of nanorods was also observed by Jia *et al.*[45,46] during the synthesis of hematite (α-Fe_2O_3) nanorods. By controlling both the phosphate concentration and hydrothermal treatment temperature, the authors were able to convert the hematite nanorods to nanotubes through the dissolution of the sharp tips toward the interior along the longitudinal axis. On the other hand, if HCl was replaced by HNO_3, a mixture of nanorods and large octahedra was obtained regardless of whether Na_3PO_4 was present in the system. Chloride ions acted as a stabilizing agent in maintaining the rod/wire structure, as was observed in the primary synthesis.

CeO_2 Nanorod/Nanowire Formation Mechanism. It is often stated that CeO_2 nanorods can only form *via* topotactic inheritance of the structure of precursors or intermediate species.[22,28,35] On the basis of this growth mechanism, CeO_2 nanorods were usually synthesized under basic conditions by topotactically inheriting the shape of initial $Ce(OH)_3$ nanorod nuclei. At a high pH, $Ce(OH)_3$ precipitates immediately because of its extremely low solubility ($K_{sp} = 7 \times 10^{-21}$, 25 °C).[47] However, in an acidic solution with pH of ~4 or lower, the $[OH^-]$ becomes less than 10^{-10} M, which makes the solubility product of $[Ce^{3+}] \times [OH^-]^3$ lower than the critical solubility constant of $Ce(OH)_3$; therefore, the formation of $Ce(OH)_3$ is no longer favorable. Instead, a more likely explanation is the direct oxidation of Ce^{3+} ions to Ce^{4+} ions by the dissolved oxygen in the synthesis mixture, leading to the formation of Ce(IV) oxide. Because of the isotropic structural property, CeO_2 nanoparticles prepared under acidic conditions are usually cubic.[39,48] It is therefore surprising to see in our system that highly stable CeO_2 nanorods were obtained under acidic conditions in a wide range of synthesis composition and conditions. Since the formation of $Ce(OH)_3$ nanorod nuclei can be excluded under acidic conditions, the CeO_2 nanorods obtained in this study were probably formed by a growth mechanism other than the structure inheritance model.

To understand the exact growth mechanism, a detailed structural analysis of CeO_2 nanorods was performed using HRTEM. Figure 4a shows the clear lattice fringes of {111} and {200} with interplanar spacings of 0.31 and 0.28 nm, indicating the cubic structure of CeO_2 nanorods with [211] growth direction. Although there is only one study reporting the synthesis of ceria nanorods with the same growth direction,[49] the feasibility of producing CeO_2 nanorods oriented along [211] was recently confirmed by Sayle *et al.*[50] using atomistic simulation. By conducting detailed morphological analysis for nanorods formed at the early stage, Du *et al.*[49] also successfully demonstrated that CeO_2 nanorods with the [211] orientation were grown by the so-called "oriented attachment" mechanism, in which adjacent nanoparticles are self-assembled by sharing a common crystallographic orientation followed by joining these particles at a planar interface, eventually leading to the development of single-crystalline anisotropic structure. HRTEM analysis of the CeO_2 nanorods obtained from a shorter time (*i.e.*, 8 h synthesis; Figure 4b) shows that, although

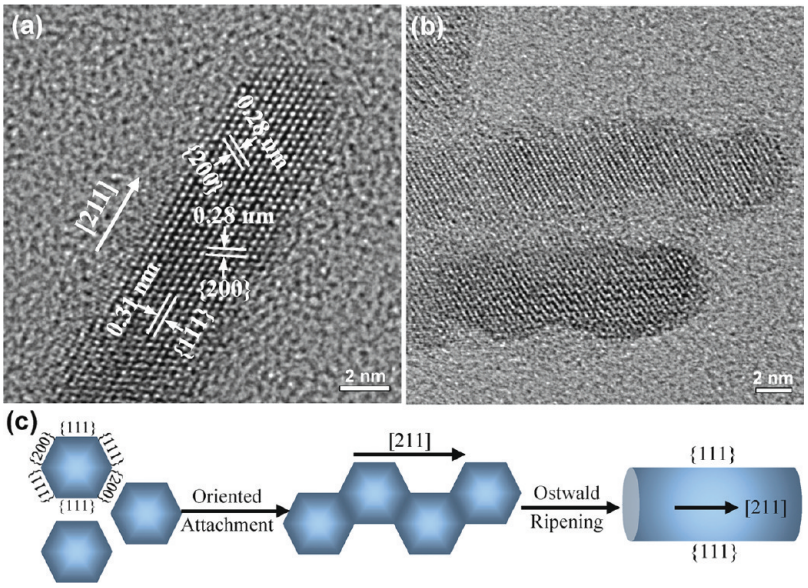

Figure 4. HRTEM analyses of CeO_2 nanorods obtained from a standard synthesis with 0.1 M $CeCl_3$ after (a) 15 h and (b) 8 h hydrothermal treatment at 220 °C; (c) schematic diagram of the formation of CeO_2 nanorods along the [211] direction *via* oriented attachment followed by Ostwald ripening.

the lattice planes are almost perfectly aligned, bottlenecks between the adjacent particles are still visible. This strongly supports the proposed oriented attachment growth mechanism. Generally, the driving force for this spontaneous oriented attachment is to reduce the overall surface energy by eliminating the surfaces at which the crystallites join. Two types of attachment pathways could occur: the attachment is aligned along the [211] direction with exposed {111} surfaces or the attachment is along the [110] direction with exposed {200} surfaces. The former would be more favorable because the CeO_2 {111} surface is the most stable surface.[51] It is therefore not surprising that we only observed CeO_2 nanorods aligned along the [211] direction in this study. A schematic diagram of CeO_2 nanorod formation by the proposed oriented attachment is shown in Figure 4c. According to this mechanism, if there is no lateral attachment, the width of the nanorods would be similar to the diameter of the initial nanoparticles in the starting solution and would not vary significantly from synthesis to synthesis. This indeed is what we observed, as shown in Figure 1 and Table 1. The same oriented attachment crystallization mechanism was also demonstrated in the syntheses of other nanomaterials such as TiO_2, ZnO, and ZnS.[52−55]

Nanorods obtained from a longer synthesis time have much smoother surfaces compared to those with shorter synthesis times (Figure 4a *vs* Figure 4b). A slight increase in the nanorod diameter upon extended treatment was also observed in our kinetic experiments (data not shown). Both suggest Ostwald ripening as the main process at the later stage of the synthesis. The CeO_2 nanorod/nanowire reconstruction in the secondary treatment could also be explained by a typical Ostwald ripening process, where the longer nanorods/nanowires were formed at the expense of dissolution of shorter ones. Clearly, both oriented attachment and Ostwald ripening operate in this system.

As the oriented attachment occurs through directed or undirected particle aggregation, it is possible that the presence of PO_4^{3-} ions favored the initial agglomeration/aggregation process. On the other hand, the presence of the hexagonal $CePO_4$ phase at the early stage of the synthesis as detected by XRD analysis (*e.g.*, 1 h synthesis in Figure 2f) suggests that the formation of $CePO_4$ nuclei cannot be excluded. It is known that $CePO_4$ can form at highly acidic conditions by the following reaction: $Ce^{3+} + H_nPO_4^{(3-n)-} \rightarrow CePO_4 + nH^+$.[56] Since only a very small amount ($1-5 \times 10^{-3}$ M) of Na_3PO_4 was added in our synthesis mixture, the PO_4^{3-} ions were exhausted rapidly during the nucleation step. The subsequent crystal growth should be attributed to the continuous precipitation of CeO_2 species, which is in agreement with our XRD analysis (Figure 2f), showing CeO_2 as the only phase in the final product. Chloride ions on the other hand might have acted as a stabilizing agent throughout the crystallization process. As reported by Wu *et al.*,[25] the adsorption of Cl^- ions could stabilize the nanorod structure of CeO_2, which would otherwise be converted into nanocubes by NO_3^- or oxygen. A similar structure-stabilizing role of Cl^- ions was also observed by Wang *et al.* during their ceria synthesis.[40] According to Kepinski *et al.*,[57] Cl^- ions, if present, tend to replace oxygen vacancies in CeO_2 and incorporate into the subsurface layer of CeO_2, thus converting CeO_2 into an

oxygen-deficient phase CeO_x. In a separate study, they also show that CeO_x obtained from the chlorine-free system reoxidized rapidly upon exposure to air but remained relatively stable in the chloride-containing system.[58] We believe that the crucial role of Cl^- ions can be attributed to their high affinity to ceria surfaces, therefore protecting the CeO_x phase against rapid oxidation and conversion to a more stable CeO_2 cubic phase. All together, our results show that it is the unique combination of PO_4^{3-} and Cl^- ions that allowed the formation of stable ceria nanorods/nanowires in a wide range of synthesis compositions and conditions.

CeO_2 Nanorod/Nanowire Dispersion for Biological Studies. Having successfully developed the hydrothermal approach to create a CeO_2 nanorod/nanowire combinatorial library, it became possible to systematically study the effects of length and aspect ratio on biological reactivity of this material. We therefore selected eight samples consisting of one CeO_2 nanocube (~7 nm, S0, Figure S5) and seven CeO_2 nanorods/nanowires with different aspect ratios (S1, S2...S7) to perform a cellular study. This selection covers the entire range of aspect ratios that were synthesized and, as discussed below, enables us to define a "critical" aspect ratio related to toxicological outcome. Common names for anisotropic shapes include rods, wires, needles, and fibers; in the following discussion, the term "rod" refers to aspect ratio of 30 and lower and "wire" refers to aspect ratios higher than 30. Accurate and reproducible biological experiments require that nanoparticles be homogeneously distributed in cell culture media. To improve the dispersion of CeO_2 nanorods and nanowires in RPMI 1640 cell culture medium, fetal bovine serum (FBS), which has been shown to be effective for stabilizing metal oxide nanoparticles in various aqueous media,[59] was selected as the dispersing agent in this study. The average hydrodynamic diameters of all eight CeO_2 nanoparticles in water and RPMI were determined using high-throughput dynamic light scattering (HT-DLS). It should be noted that hydrodynamic diameters for nonspherical particles like nanorods and nanowires are defined as the equivalent spherical diameters, that is, the diameter of a sphere with the same translational diffusion coefficient, and cannot be simply related to the exact particle sizes. Therefore, the hydrodynamic diameters measured here only represent "relative" sizes of the CeO_2 nanorods and nanowires. The DLS measurement does, however, provide a good indication of the dispersion state of high aspect ratio nanomaterials, which is confirmed by our recent study showing that HT-DLS is a valuable technique for estimating the dispersion state of multiwalled carbon nanotubes.[60] When directly suspended in serum-free RPMI medium, all CeO_2 nanorods/nanowires showed considerable agglomeration with average hydrodynamic diameters varying from 645 to 1200 nm. In contrast, when 10% FBS was added to the medium (cRPMI), the average hydrodynamic diameters were significantly reduced (by as much as a factor of 3) and achieved sizes comparable to those in water (Table 2). These results are consistent with our previous studies,[59−61] where FBS was demonstrated to be an effective dispersing agent for stabilizing many different types of nanomaterials such as TiO_2, Ag, and carbon nanotubes.

TABLE 2. Hydrodynamic Diameters of CeO_2 Nanorods with Relatively Constant Diameter (*D*) but Different Lengths (*L*) and Aspect Ratios (*R*) in Water, Serum-Free RPMI Medium, and RPMI Supplemented with 10% FBS (cRPMI) As Determined by Dynamic Light Scattering

				hydrodynamic diameter (nm)		
sample name	*L* (nm)	*D* (nm)	*R*	water	RPMI	cRPMI
S0	N/A	7	1	55 ± 4	1200 ± 53	392 ± 9
S1	33.2	8.0	4	153 ± 18	1125 ± 139	364 ± 18
S2	50.8	6.7	8	227 ± 4	808 ± 188	424 ± 24
S3	106.7	6.6	16	213 ± 43	847 ± 17	452 ± 22
S4	197.2	9.1	22	475 ± 27	749 ± 116	449 ± 27
S5	310.4	9.7	31	479 ± 27	645 ± 101	508 ± 75
S6	495.7	9.5	52	735 ± 24	913 ± 120	648 ± 76
S7	>1000	~9.5	>100	844 ± 123	899 ± 165	865 ± 22

High Aspect Ratio CeO_2 Nanorods/Nanowires Induce Cytotoxicity and IL-1β Production in THP-1 Cells. THP-1 is a human monomyelocytic leukemia cell line that has been extensively used to study inflammasome activation in response to various environmentally hazardous substances such as silica,[37,62] polystyrene particles,[63] asbestos,[37,64] and carbon nanotubes.[65] Upon treatment with phorbol 12-myristate acetate (PMA), these cells differentiate into a myeloid phenotype with the acquisition of macrophage-like properties. In a recent study,[65] we demonstrated that multiwalled carbon nanotubes could activate NALP3 inflammasome and lead to IL-1β cytokine release in THP-1 cells. These results correlate well with the *in vivo* lung fibrogenic cytokine including IL-1β production. On the basis of these findings, we selected THP-1 as a cellular model here to study the impact of high aspect ratio CeO_2 nanorods and nanowires.

Cellular viability was determined using an LDH release assay. Following cellular exposure to CeO_2 nanocubes (S0) and nanorods with aspect ratios up to 31 (S1−S5) for 24 h, no effect on cell viability was seen with doses as high as 100 μg mL^{-1}. However, when exposed to the two materials with the highest aspect ratios (S6 and S7), THP-1 cells showed a significantly higher cell death rate compared to the shorter rods (Figure 5a). A similar response was observed when assessing IL-1β levels in the cell culture supernatants: nanocubes and short nanorods induced little or no increase in IL-1β production, whereas the nanowires induced high cytokine levels (Figure 5b). Interestingly, although samples S4 and S5 with an intermediary aspect ratio of 22 and 31, respectively, did not

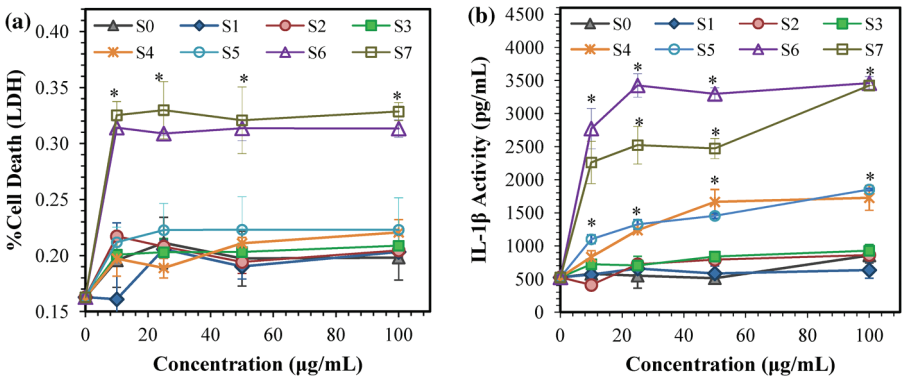

Figure 5. Cellular viability and IL-1β production in THP-1 cells following 24 h exposure to CeO_2 nanoparticles: (a) % cell death of THP-1 cells after exposed to CeO_2 nanoparticles as determined by LDH assay; (b) IL-1β production by THP-1 cells in the cell culture supernatant postexposed to CeO_2 nanoparticles. Asterisk * denotes statistical significance at $p < 0.05$ as compared to control.

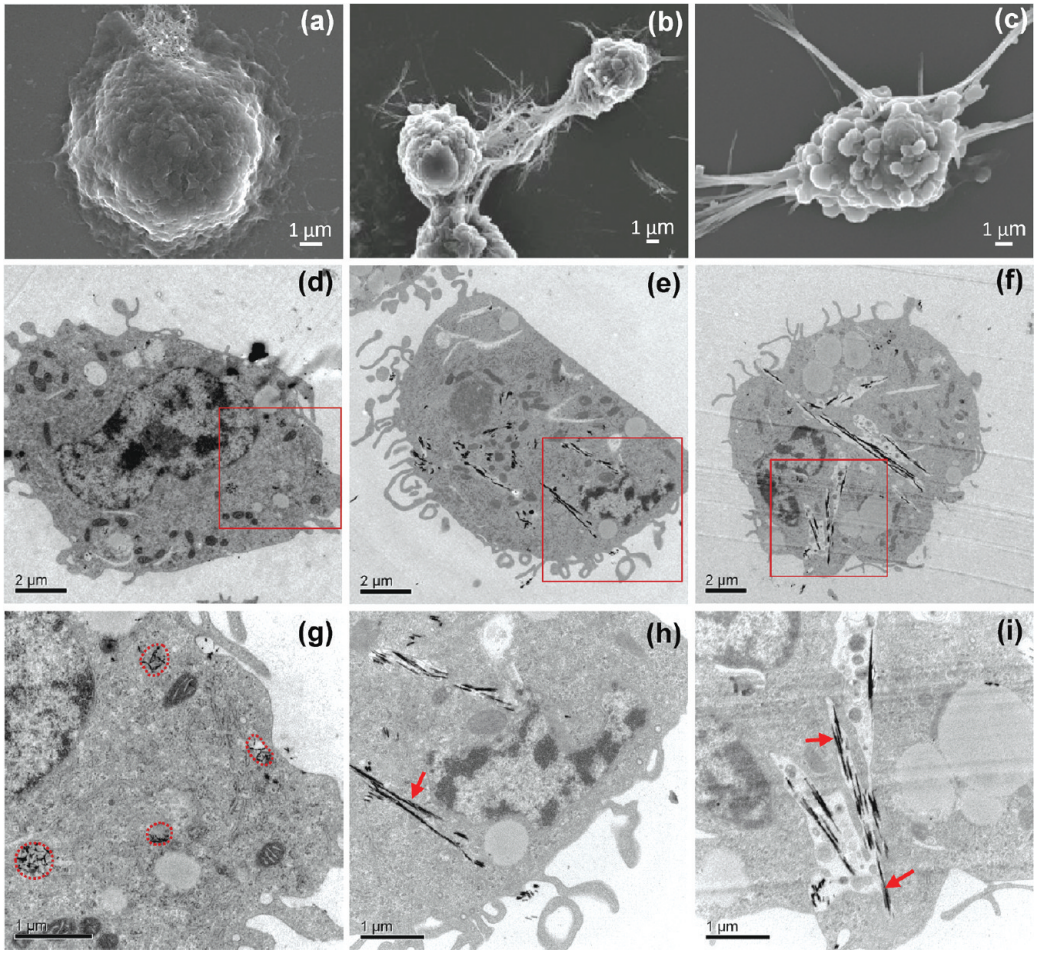

Figure 6. Ultrastructural analysis to elucidate the interaction of CeO_2 nanorods/nanowires with THP-1 cells using (a–c) SEM and (d–i) TEM. THP-1 cells were exposed to CeO_2 nanorods/nanowires for 24 h at 50 μg mL^{-1}: S2 (a,d,g); S6 (b,e,h), and S7 (c,f,i). Panels g, h, and i show a higher magnification view of the labeled square area in panels d, e, and f, respectively. The circles in panel g highlight the S2 nanorods taken up into membrane-lined subcelluar compartments as indicated by in panels h and i. The arrows indicate the "free-floating" nanorod bundles (S6 and S7) in the cytoplasm.

induce obvious cytotoxicity, these nanorods did induce a significant increase of IL-1β levels in the supernatant.

Understanding the Mechanisms of IL-1β Production. Activation of the NALP3 inflammasome by high aspect ratio materials such as uric acid crystals and asbestos fibers is dependent on lysosomal damage.[37,38,66] This damage is associated with cathepsin B release, which provides a signal for the assembly of the NALP3 inflammasome. In order to assess lysosome damage, we performed SEM (Figure 6a–c) and TEM

(Figure 6d–i) analyses to observe in more detail changes in the subcellular localization and cell morphology during interactions with rods and wires. Figure 6a shows that the THP-1 cells exposed to shorter CeO_2 nanorods (R = 8) maintained a healthy appearance in spite of abundant uptake (Figure 6d) and nanorod localization in membrane-lined compartments (Figure 6g). In contrast, the longer CeO_2 nanowires tended to bundle together, which allowed contact with the cellular surface or even piercing the surface membrane (Figure 6b,c). Intracellular S6 and S7 nanowire bundles could also be seen to pierce the endolysosomal membrane, leading some wires to be released into the cytoplasm (indicated by red arrows in Figure 6h,i). These results together with the IL-1β data (Figure 5b) suggest that the formation of CeO_2 stacking bundles with an aspect ratio $\geq$22 defines a critical length beyond which lysosomes are ruptured and lead to triggering of injurious cellular responses.[37,38,66]

In order to study the functional effects of lysosome injury by CeO_2 nanowires, we used confocal microscopy to visualize the localization of a fluorescent cathepsin B substrate, Magic Red, in THP-1 cells. Use of monosodium urate (MSU) crystals revealed that the punctate red fluorescence of Magic Red in intact lysosomes changes to diffuse spread in the cytoplasm after damage to this organelle (Figure 7A). While the short CeO_2 nanorods S0 and S2 had no effect (showing punctate red fluorescence), nanorods/nanowires with aspect ratio $\geq$22, including S4, S6, and S7, all caused significant lysosomal damage (Figure 7B). Although less quantitative than IL-1β data (Figure 5b), these results are in accordance with the cytokine data. The contribution of cathepsin B release to IL-1β production was demonstrated by suppression of cytokine production by the specific cathepsin B inhibitor, CA-074 methyl ester (Figure 8a), as well as an endocytosis inhibitor, cytochalasin D (Figure 8b), which interfered in nanowire uptake. The involvement of the inflammasome in these responses was confirmed by using NALP3$^{-/-}$ and ASC-deficient (ASC$^{-/-}$) THP-1 cells, which failed to show cytokine production in response to the materials with the highest aspect ratios, S6 and S7 (Figure 9).

An interesting observation during the study of the CeO_2 nanorods and nanowires is that the maximum length of the stacking bundles is only 6–7 μm, much less than that typically required (15–20 μm) for the induction of frustrated phagocytosis by fiber-like substances such as asbestos.[7,67] This suggests that the major impact of the aspect ratio at a shorter length scale is lysosomal damage rather than the length scale at which fiber-like materials exceed the total length of the cell, as has been suggested in the asbestos literature. It appears that a critical length of ~200 nm and aspect ratio of 22 are sufficient to achieve nanorod/nanowire stacking bundle dimensions (0.75–2 μm in length) that lead to lysosomal damage (the diameter of lysosomes was estimated to be 1.1–2.9 μm).[68]

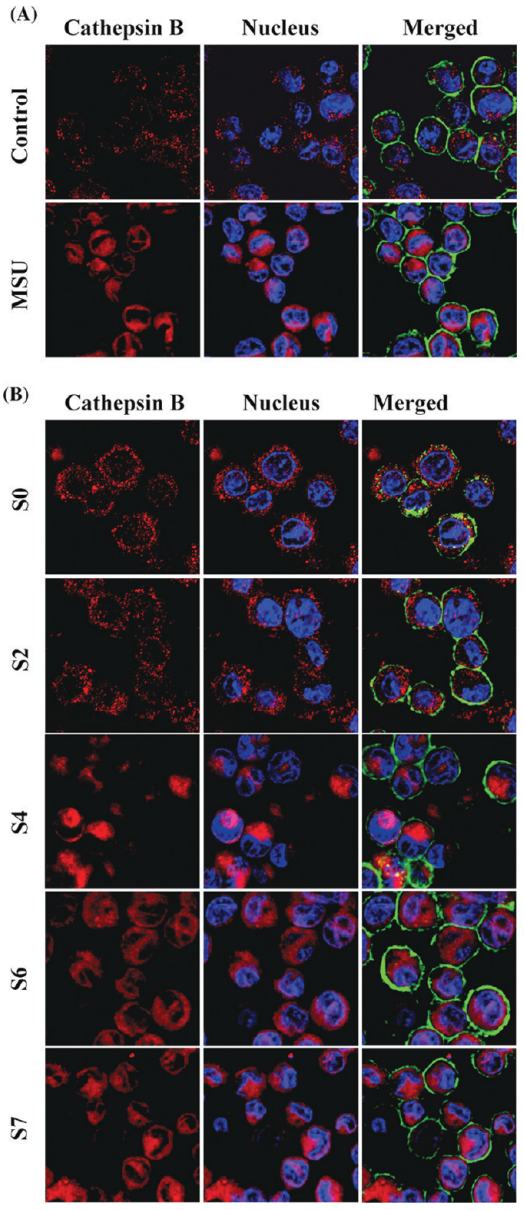

Figure 7. Comparison of the effects of CeO_2 nanorods with different aspect ratios on cathepsin B release from damaged lysosomes and the initiation of NALP3 inflammasome activation in THP-1 cells. THP-1 cells were seeded into 8-well chamber slides and incubated with CeO_2 nanorods of different aspect ratio at 80 μg mL^{-1} for 4 h in complete RPMI 1640 and then stained with Magic Red (ImmunoChemistry Technologies) for 30 min. After fixation and permeabilization, cells were stained with wheat germ agglutinin 633, and Hoechst 33342 dye, followed by visualization under a confocal 1P/FCS inverted microscope as described in the Materials and Methods section. Monosodium urate (MSU) crystals were used as the positive control. (A) Control cells exhibited intact punctate lysosomes stained by the red fluorescent cathepsin B substrate, while MSU-treated cells showed a diffuse red color in the cytoplasm as a result of lysosome damage. (B) In agreement with the cellular data in Figure 5, S0 and S2 materials had no effect on cathepsin B release compared to prominent lysosome damage by the higher aspect ratio materials (S4, S6, and S7).

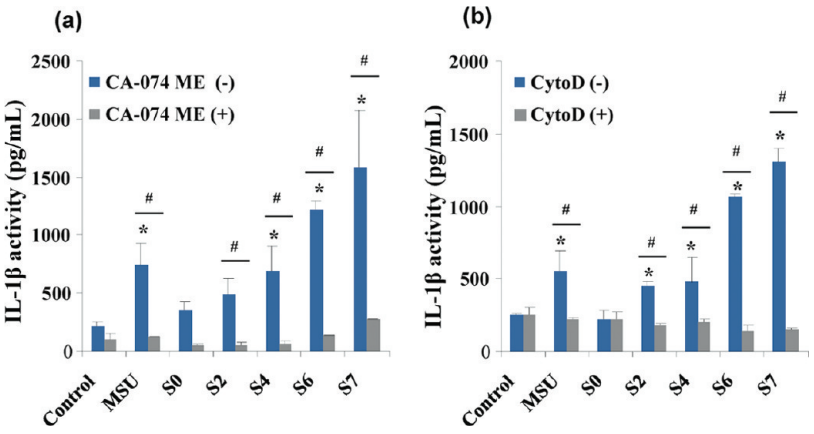

Figure 8. Use of specific inhibitors to demonstrate the involvement of the NALP3 inflammasome in IL-1β production: (a) THP-1 cells were pretreated with cathepsin B inhibitor, CA-074 methyl ester, at 10 μM for 45 min and then exposed to different aspect ratio CeO_2 nanorods at 80 μg mL^{-1} for 5 h in complete RPMI 1640. There was a statistically significant decrease in IL-1β production for S2, S4, S6, and S7. No statistical changes were found in S0; # denotes $p < 0.05$ compared to non-drug-treated control cells; * statistically significant at $p < 0.05$ compared to CA-074 ME (+) cells; #$p < 0.05$ for pairwise comparisons as shown. (b) Similar inhibition results are observed when using the endocytosis inhibitor, cytochalasin D.

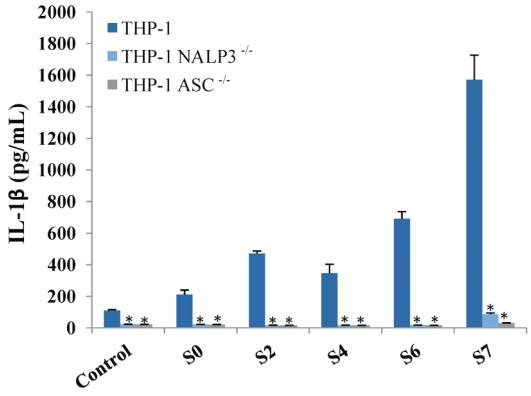

Figure 9. IL-1β production in reponse to high aspect ratio CeO_2 nanorods/nanowires is dependent on NALP3 and ASC. Wild-type THP-1, THP-1 NALP3$^{-/-}$, and THP-1 ASC$^{-/-}$ cells were exposed to CeO_2 nanorods/nanowires of different aspect ratio at 80 μg mL^{-1} for 5 h in complete RPMI 1640. There was a statistically significant decrease in IL-1β production in THP-1 NALP3$^{-/-}$ and THP-1 ASC$^{-/-}$ cells compared to wild-type THP-1 cells for all nanorods/nanowires tested. The * denotes $p < 0.05$ compared to wild-type THP-1 cells.

The relatively low length scale and aspect ratio that lead to cellular toxicity appear to be reliant on the relatively small diameters (6−10 nm) of the hazardous CeO_2 nanorods/nanowires. When these high aspect ratio materials are very thin, the center-to-center distance between them becomes extremely short during their side-by-side alignment as opposed to end-to-end stacking; this makes the energetic forces like van der Waals and dipole−dipole attractions much stronger. As the rods get longer, the attraction between parallel-aligned nanorods can be several orders of magnitude higher than that between nanorods oriented end-to-end, therefore favoring the formation of stacking bundles like those seen in samples S6 and S7 in Figure 6. Maximization of entropy by minimizing the excluded volume per particle in the bundle can be another important driving force for the side-by-side alignment. A recent study by Nagai *et al.*[69] showed that thin multiwalled carbon nanotubes (MWCNTs, diameter ~50 nm) are more cytotoxic, inflammogenic, and carcinogenic than thick MWCNTs (diameter ~150 nm) of similar lengths. Although we did not investigate the effect of varying diameters in this study, our results suggest that thin nanowires may contribute to lysosomal damage at shorter lengths and lower aspect ratios than traditionally described for fiber-like substances such as asbestos. However, it still needs to be determined whether the CeO_2 nanowires induce chronic granulomatous inflammation and pulmonary fibrosis similar to asbestos and carbon nanotubes. This will be determined by the use of rodent lung instillation studies, which is important from the perspective of the possible inhalation toxicology of CeO_2 emissions from gasoline that is supplemented with this material. While generally we have found spherical CeO_2 nanoparticles to be relatively innoxious in the lung,[70] the injury potential of this material may change considerably when the exposure occurs to high aspect ratio CeO_2 nanowires. Other important physicochemical properties such as crystallinity, surface area, and structural defects may also impact the critical length and aspect ratio.

CONCLUSIONS

In summary, we have demonstrated a very effective surfactant- and organic template-free hydrothermal approach for synthesizing CeO_2 nanorods and nanowires. By controlling synthesis compositions and conditions, the nanorod/nanowire aspect ratios were precisely controlled and finely tuned in a very wide range. Efforts were also made to understand the crystallization mechanism in both primary and secondary

synthesis systems. High-resolution TEM analysis suggests that single-crystalline CeO_2 nanorods/nanowires obtained in the primary syntheses were formed along the [211] growth direction by the oriented attachment mechanism followed by Ostwald ripening. The CeO_2 nanorods/nanowires could also be reconstructed into even longer ones by an additional secondary hydrothermal treatment, in which the longer nanorods/nanowires were formed at the expense of dissolution of shorter ones, which again is explained by a typical Ostwald ripening process. Both phosphate and chloride ions were shown to play critical roles in obtaining one-dimensional CeO_2 nanostructures in both primary and secondary experiments. The successful creation of a collection of CeO_2 nanorod/nanowires in the form of a combinatorial library has allowed us, for the first time, to systematically dissect the role of length and aspect ratio of this material in a biological setting. The *in vitro* toxicity studies showed that the short CeO_2 nanorods with R = 1−16 were all nontoxic. The nanorods with intermediary aspect ratios, R = 22 and 31, did not cause any obvious cell death but did induce IL-1β production. The two highest aspect ratio nanowires led to significant IL-1β release as well as cell death. The relatively low critical length (200 nm) and aspect ratio (R = 22) identified here could be associated with the ease of forming stacking bundles for thin (6−10 nm) nanorods/nanowires due to strong van der Waals and dipole−dipole attractions between parallel-aligned rods/wires. Although we did not investigate the diameter effect in this study, our results do suggest that thin nanorods/nanowires may induce inflammasome activation at much shorter lengths and lower aspect ratios. The classic "length-dependent" theory should be more rigorously tested by taking into account the effects of diameter as well as other important physicochemical properties.

MATERIALS AND METHODS

Hydrothermal Synthesis of CeO_2 Nanoparticles. All CeO_2 nanoparticles were prepared using the traditional hydrothermal synthesis method. In a typical CeO_2 nanorod synthesis, 0.1863−4.4710 g of cerium(III) chloride (99.9%, $CeCl_3 \cdot 7H_2O$, Sigma-Aldrich) was dissolved in 15 mL of deionized water in a 60 mL high-density polyethylene (HDPE) bottle to form solution I. To prepare solution II, 0.0272 g of sodium phosphate tribasic hexahydrate (≥97%, $Na_3PO_4 \cdot 6H_2O$, Sigma-Aldrich) was dissolved in 5 mL of deionized water in another 60 mL HDPE bottle. Solution I was then poured into solution II, and the resulting synthesis mixture was vigorously mixed for ∼5 min before transferring into a 23 mL Teflon-lined stainless steel autoclave. All reactions were carried out in an electric oven under autogenous pressure and static conditions. The pH values of the initial synthesis mixture as well as the final product were measured using a Mettler Toledo SevenEasy pH meter. After the crystallization was complete, the autoclaves were immediately cooled in a water bath. The fresh white precipitates were separated by centrifugation and washed with deionized water and ethanol alternatively for three cycles to remove ionic remnants. The final product was dried at 60 °C overnight under ambient environment. CeO_2 nanocubes were prepared using a published procedure[28] with a synthesis mixture containing 0.1 M cerium(III) nitride and 0.01 M sodium hydroxide. The crystallization was carried out at 140 °C for 24 h under autogenous pressure and static conditions. The final product was centrifuged and thoroughly washed using the same method as that for CeO_2 nanorods.

Physical and Chemical Characterization. Transmission electron microscopy (TEM, JEOL 1200 EX, accelerating voltage 80 kV) was used to observe the morphology and to determine the primary size of CeO_2 nanoparticles. Samples were prepared by placing a drop of the CeO_2 aqueous suspension on a carbon-coated TEM grid and waiting until all of the water evaporated. High-resolution transmission electron microscopic (HRTEM) analyses was performed using a FEI Titan 80/300 microscope equipped with a Cs corrector for the objective lens, high-angle annular dark-field detector (HAADF), GATAN postcolumn imaging filter, and a cold field emission gun operated at an accelerating voltage of 300 kV. X-ray powder diffraction (XRD, Panalytical X'Pert Pro diffractometer, Cu Kα radiation) was utilized for phase identification and to determine the percent crystallinity in the final CeO_2 product. The XRD pattern was collected with a step size of 0.02° and counting time of 0.5 s per step over a range of 20−80° 2θ. High-throughput dynamic light scattering (HT-DLS, Dynapro Plate Reader, Wyatt Technology) was performed to determine the particle size and size distribution of the CeO_2 nanoparticles in water and the cell culture medium following the procedure developed in our previous study on TiO_2.[59]

THP-1 Cellular Culture and Co-incubation with CeO_2 Nanorods. THP-1 cells were suspended in RPMI 1640 medium supplemented with 10% fetal bovine serum in 75 cm^2 flasks. Before exposure to CeO_2 nanoparticles, THP-1 cells were pretreated with 1 $\mu g\ mL^{-1}$ phorbol 12-myristate acetate (PMA) overnight and primed with 10 ng mL^{-1} lipopolysaccharide (LPS). LPS is necessary because, upon the addition of LPS, THP-1 cells undergo programmed differentiation. The LPS molecule is recognized by Toll-like receptor 4 (TLR4) residing on the cell membrane, which further leads to NF-κB activation through adaptor protein MyD88, and the production of pro-form interleukin 1β (pro-IL-1β), which will be presented for caspase cleavage to produce mature IL-1β. Then aliquots of 2×10^4 primed cells were cultured in 0.2 mL of medium with CeO_2 nanoparticles in 96-well plates (Costar, Corning, NY, USA) at 37 °C for 24 h. All of the CeO_2 nanoparticle suspensions were freshly prepared. After 24 h of culture, the supernatants were collected for the measurement of LDH levels and IL-1β activity. THP-1 NALP3$^{-/-}$ and THP-1ASC$^{-/-}$ cells were obtained from InvivoGen. Cells were grown in RPMI 1640 media supplemented with 10% (v/v) fetal bovine serum (FBS), 200 $\mu g\ mL^{-1}$ HygroGold, 100 $\mu g\ mL^{-1}$ Normocin, and 50 U/mL 50 $\mu g\ mL^{-1}$ penicillin-streptomycin before exposure to CeO_2 nanoparticles.

Electron Microscopy Analysis of Cell−Nanoparticle Interaction. THP-1 cells were exposed to CeO_2 nanorods suspended in RPMI 1640 at 50 $\mu g\ mL^{-1}$ for 24 h. For scanning electron microscope (SEM) imaging, the exposed cells were placed on a glass substrate, fixed in 2.5% glutaraldehyde, and dehydrated in a graded ethanol series. Once in 100% ethanol, the mounted cells were critically point dried in a Balzers CPD030, mounted on an aluminum stub, and sputter coated with gold/palladium in a Pelco model 3 sputter coater. The cells were imaged using a JEOL JSM-67 field emission scanning electron microscope at 10 kV. For transmission electron microscope (TEM) analysis, after exposure to CeO_2 nanoparticles, the cells were fixed with 2% glutaraldehyde in 0.1 M phosphate-buffered saline (PBS) and washed. After postfixation in 1% osmium tetroxide containing PBS for 1 h, the cells were dehydrated in a graded series of ethanol, treated with propylene oxide, and embedded in Epon. Approximately 50−70 nm thick sections were cut on a Reichert-Jung Ultracut E ultramicrotome and picked up on Formvar-coated copper grids. The sections were stained with uranyl acetate and Reynolds lead citrate and examined on a JEOL

100 CX transmission electron microscope at 80 kV in the UCLA BRI Electron Microscopy Core.

Determination of Cytotoxicity. Cellular viability was determined using LDH release assays. After incubation with nanoparticles at a dose range of 10, 25, 50, and 100 μg mL^{-1} for 24 h at 37 °C, the cell supernatants from control and treated samples were collected and centrifuged at 15 000*g* for 10 min. LDH activity was measured by using a commercial kit (CytoTox 96, Promega, Madison, WI, USA). The LDH levels were determined by measuring optical absorbance at 490 nm in 96-well plates. Cell lysates were used for assessing the total cellular content, and the percentage LDH release was calculated by dividing the LDH levels in the supernatant by the total LDH content in the cell lysate.

ELISA for IL-1β Activity Quantification. The IL-1β activity in the THP-1 culture supernatant was determined by an OptEIA (BD Biosciences, CA) according to the manufacturer's instructions. A 96-well plate was coated with monoclonal anti-IL-1β and the captured growth factor detected by polyclonal anti-IL-1β conjugated to horseradish peroxidase. Absorbance was measured at 450 nm using a plate reader (SpectroMax M5e, Molecular Devices Corp., Sunnyvale, CA, USA). Results were expressed as pg per mL.

Lysosomal Damage and Cathepsin B Release Identified by Magic Red. Primed THP-1 cells (1×10^5) were seeded into each of an 8-well chamber and incubated with CeO_2 nanocubes and nanorods at 80 μg mL^{-1} for 4 h in RPMI 1640. After treatment, cells were stained with Magic Red (ImmunoChemistry Technologies) at 26 nM for 1 h. Following fixation in 4% paraformaldehyde for 1 h in PBS and three-time careful washes with PBS, cell membranes and nucleus were co-stained with 5 μg/mL AlexaFluor633-conjugated wheat germ agglutinin (WGA) and Hoechst 33342 in PBS for 30 min. The chamber was then visualized under a confocal microscope (Leica Confocal 1P/FCS) in the UCLA/CNSI Advanced Light Microscopy/Spectroscopy Shared Facility. High-magnification images were obtained with the 100× objective. Cells without CeO_2 treatment were used as control. The monosodium urate (MSU) crystal was used as the positive control.

NALP 3 Inflammasome Inhibition Studies. Differentiated and primed THP-1 cells were seeded into a 96-well plate at the density of 2.5×10^4 in 0.2 mL complete RPMI 1640 medium. The cells were precultured with CA-074 methyl ester (cathepsin B inhibitor at 10 μM) or cytochalasin D (endocytosis inhibitor at 5 μg mL^{-1}) for 45 min. Following the preculture, the medium was exchanged into fresh RPMI 1640 that contained 80 μg/mL CeO_2 nanocubes and nanorods, one of the chemical inhibitors (CA-074 methyl ester, or cytochalasin D) for a further 5 h. Then the supernatant was collected to measure the IL-1β production by ELISA.

Conflict of Interest: The authors declare no competing financial interest.

Acknowledgment. This work is supported by the U.S. Public Health Service Grants (RO1 ES016746 and U19 ES019528). Infrastructure support was also provided by the National Science Foundation and the Environmental Protection Agency to the UC Center for Environmental Implications of Nanotechnology under Cooperative Agreement Number DBI-0830117. The authors acknowledge the use of TEM instruments at the Electron Imaging Center for NanoMachines supported by NIH (1S10RR23057 to Z.H.Z.) and CNSI at UCLA. Z.J. thanks Mathew Mecklenburg for help with HRTEM analysis.

Supporting Information Available: XRD patterns of CeO_2 nanorods obtained with different initial $CeCl_3$ concentrations (Figure S1), TEM images of CeO_2 nanorods and nanowires obtained from lower pH synthesis (Figure S2), seeding (Figure S3) and kinetic experiments in the secondary hydrothermal treatment (Figure S4), TEM images of CeO_2 nanocubes (Figure S5). This material is available free of charge *via* the Internet at http://pubs.acs.org.

REFERENCES AND NOTES

1. Tans, S. J.; Verschueren, A. R. M.; Dekker, C. Room-Temperature Transistor Based on a Single Carbon Nanotube. *Nature* **1998**, *393*, 49–52.
2. Huang, M. H.; Mao, S.; Feick, H.; Yan, H.; Wu, Y.; Kind, H.; Weber, E.; Russo, R.; Yang, P. Room-Temperature Ultraviolet Nanowire Nanolasers. *Science* **2001**, *292*, 1897–1899.
3. Ju, S.; Lee, K.; Janes, D. B.; Yoon, M. H.; Facchetti, A.; Marks, T. J. Low Operating Voltage Single ZnO Nanowire Field-Effect Transistors Enabled by Self-Assembled Organic Gate Nanodielectrics. *Nano Lett.* **2005**, *5*, 2281–2286.
4. Favier, F.; Walter, E. C.; Zach, M. P.; Benter, T.; Penner, R. M. Hydrogen Sensors and Switches from Electrodeposited Palladium Mesowire Arrays. *Science* **2001**, *293*, 2227–2231.
5. Wang, X.; Song, J.; Liu, J.; Wang, Z. L. Direct-Current Nanogenerator Driven by Ultrasonic Waves. *Science* **2007**, *316*, 102–105.
6. Meng, H.; Yang, S.; Li, Z.; Xia, T.; Chen, J.; Ji, Z.; Zhang, H.; Wang, X.; Lin, S.; Huang, C.; *et al.* Aspect Ratio Determines the Quantity of Mesoporous Silica Nanoparticle Uptake by a Small GTPase-Dependent Macropinocytosis Mechanism. *ACS Nano* **2011**, *5*, 4434–4447.
7. Oberdorster, G.; Stone, V.; Donaldson, K. Toxicology of Nanoparticles: A Historical Perspective. *Nanotoxicology* **2007**, *1*, 2–25.
8. Poland, C. A.; Duffin, R.; Kinloch, I.; Maynard, A.; Wallace, W. A. H.; Seaton, A.; Stone, V.; Brown, S.; MacNee, W.; Donaldson, K. Carbon Nanotubes Introduced into the Abdominal Cavity of Mice Show Asbestos-like Pathogenicity in a Pilot Study. *Nat. Nanotechnol.* **2008**, *3*, 423–428.
9. Castranova, V.; Blake, T.; Schwegler-Berry, D.; Baron, P.; Deye, G. J.; Li, C. H.; Jones, W. Effect of Fiber Length on Glass Microfiber Cytotoxicity. *J. Toxicol. Environ. Health, Part A* **1998**, *54*, 243–259.
10. Fubini, B.; Tomatis, M.; Turci, F.; Ceschino, R.; Riganti, C.; Gazzano, E.; Martra, G.; Ghigo, D. High Aspect Ratio Materials: Role of Surface Chemistry *vs*. Length in the Historical "Long and Short Amosite Asbestos Fibers". *Inhal. Toxicol.* **2010**, *22*, 984–998.
11. Donaldson, K.; Poland, C. A.; Duffin, R.; Kinloch, I.; Maynard, A.; Wallace, W. A. H.; Seaton, A.; Stone, V.; Brown, S.; MacNee, W. Carbon Nanotubes Introduced into the Abdominal Cavity of Mice Show Asbestos-like Pathogenicity in a Pilot Study. *Nat. Nanotechnol.* **2008**, *3*, 423–428.
12. Palomaki, J.; Valimaki, E.; Sund, J.; Vippola, M.; Clausen, P. A.; Jensen, K. A.; Savolainen, K.; Matikainen, S.; Alenius, H. Long, Needle-like Carbon Nanotubes and Asbestos Activate the NLRP3 Inflammasome through a Similar Mechanism. *ACS Nano* **2011**, *5*, 6861–6870.
13. Nelson, S. M.; Mahmoud, T.; Beaux, M., II; Shapiro, P.; McIlroy, D. N.; Stenkamp, D. L. Toxic and Teratogenic Silica Nanowires in Developing Vertebrate Embryos. *Nanomedicine* **2010**, *6*, 93–102.
14. Hamilton, R. F.; Wu, N.; Porter, D.; Buford, M.; Wolfarth, M.; Holian, A. Particle Length-Dependent Titanium Dioxide Nanomaterials Toxicity and Bioactivity. *Part. Fibre Toxicol.* **2009**, *6*, 35.
15. Muller, K. H.; Kulkarni, J.; Motskin, M.; Goode, A.; Winship, P.; Skepper, J. N.; Ryan, M. P.; Porter, A. E. pH-Dependent Toxicity of High Aspect Ratio ZnO Nanowires in Macrophages Due to Intracellular Dissolution. *ACS Nano* **2010**, *4*, 6767–6779.
16. Hickman, J. J.; Das, M.; Patil, S.; Bhargava, N.; Kang, J. F.; Riedel, L. M.; Seal, S. Auto-Catalytic Ceria Nanoparticles Offer Neuroprotection to Adult Rat Spinal Cord Neurons. *Biomaterials* **2007**, *28*, 1918–1925.
17. Tarnuzzer, R. W.; Colon, J.; Patil, S.; Seal, S. Vacancy Engineered Ceria Nanostructures for Protection from Radiation-Induced Cellular Damage. *Nano Lett.* **2005**, *5*, 2573–2577.
18. Self, W. T.; Korsvik, C.; Patil, S.; Seal, S. Superoxide Dismutase Mimetic Properties Exhibited by Vacancy Engineered Ceria Nanoparticles. *Chem. Commun.* **2007**, 1056–1058.
19. Perez, J. M.; Asati, A.; Nath, S.; Kaittanis, C. Synthesis of Biocompatible Dextran-Coated Nanoceria with pH-Dependent Antioxidant Properties. *Small* **2008**, *4*, 552–556.
20. Laberty-Robert, C.; Long, J. W.; Lucas, E. M.; Pettigrew, K. A.; Stroud, R. M.; Doescher, M. S.; Rolison, D. R. Sol–Gel-Derived

Ceria Nanoarchitectures: Synthesis, Characterization, and Electrical Properties. *Chem. Mater.* **2006**, *18*, 50–58.
21. Wu, G. S.; Xie, T.; Yuan, X. Y.; Cheng, B. C.; Zhan, L. D. An Improved Sol−Gel Template Synthetic Route to Large-Scale CeO_2 Nanowires. *Mater. Res. Bull.* **2004**, *39*, 1023–1028.
22. Zhang, D. S.; Pan, C. S.; Shi, L. Y.; Fang, J. H. Template-Free Synthesis, Controlled Conversion, and Co Oxidation Properties of CeO_2 Nanorods, Nanotubes, Nanowires, and Nanocubes. *Eur. J. Inorg. Chem.* **2008**, 2429–2436.
23. Xing, X. R.; Yan, L.; Yu, R. B.; Chen, J. Template-Free Hydrothermal Synthesis of CeO_2 Nano-Octahedrons and Nanorods: Investigation of the Morpholog Evolution. *Cryst. Growth Des.* **2008**, *8*, 1474–1477.
24. Yu, R.; Yan, L.; Zheng, P.; Chen, J.; Xing, X. Controlled Synthesis of CeO_2 Flower-like and Well-Aligned Nanorod Hierarchical Architectures by a Phosphate-Assisted Hydrothermal Route. *J. Phys. Chem. C* **2008**, *112*, 19896–19900.
25. Wu, Q.; Zhang, F.; Xiao, P.; Tao, H. S.; Wang, X. Z.; Hu, Z.; Lu, Y. N. Great Influence of Anions for Controllable Synthesis of CeO_2 Nanostructures: From Nanorods to Nanocubes. *J. Phys. Chem. C* **2008**, *112*, 17076–17080.
26. Pan, C.; Zhang, D.; Shi, L. CTAB Assisted Hydrothermal Synthesis, Controlled Conversion and Co Oxidation Properties of CeO_2 Nanoplates, Nanotubes, and Nanorods. *J. Solid State Chem.* **2008**, *181*, 1298–1306.
27. Yuan, Z. Y.; Vantomme, A.; Du, G. H.; Su, B. L. Surfactant-Assisted Large-Scale Preparation of Crystalline CeO_2 Nanorods. *Langmuir* **2005**, *21*, 1132–1135.
28. Mai, H.-X.; Sun, L.-D.; Zhang, Y.-W.; Si, R.; Feng, W.; Zhang, H.-P.; Liu, H.-C.; Yan, C.-H. Shape-Selective Synthesis and Oxygen Storage Behavior of Ceria Nanopolyhedra, Nanorods, and Nanocubes. *J. Phys. Chem. B* **2005**, *109*, 24380–24385.
29. Lin, H. L.; Wu, C. Y.; Chiang, R. K. Facile Synthesis of CeO_2 Nanoplates and Nanorods by [100] Oriented Growth. *J. Colloid Interface Sci.* **2010**, *341*, 12–17.
30. Chen, L. Q.; Sun, C. W.; Li, H.; Zhang, H. R.; Wang, Z. X. Controlled Synthesis of CeO_2 Nanorods by a Solvothermal Method. *Nanotechnology* **2005**, *16*, 1454–1463.
31. Xing, X. R.; Yan, L.; Yu, R. B.; Deng, J. X.; Chen, J.; Liu, G. R. Facile Alcohothermal Synthesis of Large-Scale Ceria Nanowires with Organic Surfactant Assistance. *Physica B* **2007**, *390*, 59–64.
32. Yada, M.; Sakai, S.; Torikai, T.; Watari, T.; Furuta, S.; Katsuki, H. Cerium Compound Nanowires and Nanorings Templated by Mixed Organic Molecules. *Adv. Mater.* **2004**, *16*, 1222–1226.
33. Tang, C.; Bando, Y.; Liu, B.; Golberg, D. Cerium Oxide Nanotubes Prepared from Cerium Hydroxide Nanotubes. *Adv. Mater.* **2005**, *17*, 3005–3009.
34. Fu, X. Q.; Wang, C.; Yu, H. C.; Wang, Y. G.; Wang, T. H. Fast Humidity Sensors Based on CeO_2 Nanowires. *Nanotechnology* **2007**, *18*, 145503/1–145503/4.
35. Zhou, K. B.; Yang, Z. Q.; Yang, S. Highly Reducible CeO_2 Nanotubes. *Chem. Mater.* **2007**, *19*, 1215–1217.
36. Wu, N.-C.; Shi, E.-W.; Zheng, Y.-Q.; Li, W.-J. Effect of pH of Medium on Hydrothermal Synthesis of Nanocrystalline Cerium(IV) Oxide Powders. *J. Am. Ceram. Soc.* **2002**, *85*, 2462–2468.
37. Tschopp, J.; Dostert, C.; Petrilli, V.; Van Bruggen, R.; Steele, C.; Mossman, B. T. Innate Immune Activation through NALP3 Inflammasome Sensing of Asbestos and Silica. *Science* **2008**, *320*, 674–677.
38. Tschopp, J.; Schroder, K. NLRP3 Inflammasome Activation: The Convergence of Multiple Signalling Pathways on ROS Production? *Nat. Rev. Immunol.* **2010**, *10*, 210–215.
39. Hirano, M.; Kato, E. Hydrothermal Synthesis of Cerium(IV) Oxide. *J. Am. Ceram. Soc.* **1996**, *79*, 777–780.
40. Wang, W.; Howe, J. Y.; Li, Y. A.; Qiu, X. F.; Joy, D. C.; Paranthaman, M. P.; Doktycz, M. J.; Gu, B. H. A Surfactant and Template-Free Route for Synthesizing Ceria Nanocrystals with Tunable Morphologies. *J. Mater. Chem.* **2010**, *20*, 7776–7781.
41. Mullin, J. W. *Crystallization*; Butterworths: London, 1961; p ix, 268 pp.
42. Murphy, C. J.; Gole, A. Seed-Mediated Synthesis of Gold Nanorods: Role of the Size and Nature of the Seed. *Chem. Mater.* **2004**, *16*, 3633–3640.
43. Ji, Z.; Warzywoda, J.; Sacco, A. Competitive Nucleation and Growth in Seeded Batch Crystallization of Titanosilicate Ets-10 Using $Ti(SO_4)_2$. *Microporous Mesoporous Mater.* **2005**, *81*, 201–210.
44. Eychmuller, A.; Ziegler, C. Seeded Growth Synthesis of Uniform Gold Nanoparticles with Diameters of 15−300 nm. *J. Phys. Chem. C* **2011**, *115*, 4502–4506.
45. Jia, C. J.; Sun, L. D.; Yan, Z. G.; You, L. P.; Luo, F.; Han, X. D.; Pang, Y. C.; Zhang, Z.; Yan, C. H. Iron Oxide Nanotubes - Single-Crystalline Iron Oxide Nanotubes. *Angew. Chem., Int. Ed.* **2005**, *44*, 4328–4333.
46. Jia, C. J.; Sun, L. D.; Luo, F.; Han, X. D.; Heyderman, L. J.; Yan, Z. G.; Yan, C. H.; Zheng, K.; Zhang, Z.; Takano, M.; *et al.* Large-Scale Synthesis of Single-Crystalline Iron Oxide Magnetic Nanorings. *J. Am. Chem. Soc.* **2008**, *130*, 16968–16977.
47. Zhou, X. D.; Huebner, W.; Anderson, H. U. Processing of Nanometer-Scale CeO_2 Particles. *Chem. Mater.* **2003**, *15*, 378–382.
48. Hirano, M.; Inagaki, M. Preparation of Monodispersed Cerium(IV) Oxide Particles by Thermal Hydrolysis: Influence of the Presence of Urea and Gd Doping on Their Morphology and Growth. *J. Mater. Chem.* **2000**, *10*, 473–477.
49. Du, N.; Zhang, H.; Chen, B. G.; Ma, X. Y.; Yang, D. R. Ligand-Free Self-Assembly of Ceria Nanocrystals into Nanorods by Oriented Attachment at Low Temperature. *J. Phys. Chem. C* **2007**, *111*, 12677–12680.
50. Sayle, D. C.; Sayle, T. X. T.; Inkson, B. J.; Karakoti, A.; Kumar, A.; Molinari, M.; Mobus, G.; Parker, S. C.; Seal, S. Mechanical Properties of Ceria Nanorods and Nanochains; the Effect of Dislocations, Grain-Boundaries and Oriented Attachment. *Nanoscale* **2011**, *3*, 1823–1837.
51. Sayle, D. C.; Maicaneanu, S. A.; Watson, G. W. Atomistic Models for CeO_2(111), (110), and (100) Nanoparticles, Supported on Yttrium-Stabilized Zirconia. *J. Am. Chem. Soc.* **2002**, *124*, 11429–11439.
52. Penn, R. L.; Banfield, J. F. Imperfect Oriented Attachment: Dislocation Generation in Defect-Free Nanocrystals. *Science* **1998**, *281*, 969–971.
53. Hyeon, T.; Yu, J. H.; Joo, J.; Park, H. M.; Baik, S. I.; Kim, Y. W.; Kim, S. C. Synthesis of Quantum-Sized Cubic ZnS Nanorods by the Oriented Attachment Mechanism. *J. Am. Chem. Soc.* **2005**, *127*, 5662–5670.
54. Weller, H.; Pacholski, C.; Kornowski, A. Self-Assembly of ZnO: From Nanodots to Nanorods. *Angew. Chem., Int. Ed.* **2002**, *41*, 1188–1191.
55. Leite, E. R.; Lee, E. J. H.; Ribeiro, C.; Longo, E. Oriented Attachment: An Effective Mechanism in the Formation of Anisotropic Nanocrystals. *J. Phys. Chem. B* **2005**, *109*, 20842–20846.
56. Zhang, Y. J.; Guan, H. M. Hydrothermal Synthesis and Characterization of Hexagonal and Monoclinic $CePO_4$ Single-Crystal Nanowires. *J. Cryst. Growth* **2003**, *256*, 156–161.
57. Kepinski, L.; Okal, J. Occurrence and Mechanism of Formation of CeOCl in Pd/CeO_2 Catalysts. *J. Catal.* **2000**, *192*, 48–53.
58. Kepinski, L.; Wolcyrz, M.; Okal, J. Effect of Chlorine on Microstructure and Activity of Pd/CeO_2 Catalysts. *J. Chem. Soc., Faraday Trans.* **1995**, *91*, 507–515.
59. Ji, Z.; Jin, X.; George, S.; Xia, T.; Meng, H.; Wang, X.; Suarez, E.; Zhang, H.; Hoek, E. M.; Godwin, H.; *et al.* Dispersion and Stability Optimization of TiO_2 Nanoparticles in Cell Culture Media. *Environ. Sci. Technol.* **2010**, *44*, 7309–7314.
60. Wang, X.; Xia, T.; Ntim, S. A.; Ji, Z.; George, S.; Meng, H.; Zhang, H.; Castranova, V.; Mitra, S.; Nel, A. E. Quantitative Techniques for Assessing and Controlling the Dispersion and Biological Effects of Multiwalled Carbon Nanotubes in Mammalian Tissue Culture Cells. *ACS Nano* **2010**, *4*, 7241–7252.
61. George, S.; Xia, T. A.; Rallo, R.; Zhao, Y.; Ji, Z. X.; Lin, S. J.; Wang, X.; Zhang, H. Y.; France, B.; Schoenfeld, D.; *et al.* Use

of a High-Throughput Screening Approach Coupled with *In Vivo* Zebrafish Embryo Screening To Develop Hazard Ranking for Engineered Nanomaterials. *ACS Nano* **2011**, *5*, 1805–1817.
62. Morishige, T.; Yoshioka, Y.; Inakura, H.; Tanabe, A.; Yao, X.; Narimatsu, S.; Monobe, Y.; Imazawa, T.; Tsunoda, S.; Tsutsumi, Y.; *et al.* The Effect of Surface Modification of Amorphous Silica Particles on NLRP3 Inflammasome Mediated Il-1β Production, ROS Production and Endosomal Rupture. *Biomaterials* **2010**, *31*, 6833–6842.
63. Lunov, O.; Syrovets, T.; Loos, C.; Beil, J.; Delacher, M.; Tron, K.; Nienhaus, G. U.; Musyanovych, A.; Mailander, V.; Landfester, K.; *et al.* Differential Uptake of Functionalized Polystyrene Nanoparticles by Human Macrophages and a Monocytic Cell Line. *ACS Nano* **2011**, *5*, 1657–1669.
64. Bonner, J. C. Regulation of PDGF and Its Receptors in Fibrotic Diseases. *Cytokine Growth Factor Rev.* **2004**, *15*, 255–273.
65. Wang, X.; Xia, T.; Ntim, S. A.; Ji, Z. X.; Lin, S. J.; Meng, H.; Chung, C. H.; George, S.; Zhang, H. Y.; Wang, M. Y.; *et al.* Dispersal State of Multiwalled Carbon Nanotubes Elicits Profibrogenic Cellular Responses That Correlate with Fibrogenesis Biomarkers and Fibrosis in the Murine Lung. *ACS Nano* **2011**, *5*, 9772–9787.
66. Tschopp, J.; Schroder, K.; Zhou, R. B. The NLRP3 Inflammasome: A Sensor for Metabolic Danger? *Science* **2010**, *327*, 296–300.
67. Donaldson, K.; Murphy, F. A.; Duffin, R.; Poland, C. A. Asbestos, Carbon Nanotubes and the Pleural Mesothelium: A Review of the Hypothesis Regarding the Role of Long Fibre Retention in the Parietal Pleura, Inflammation and Mesothelioma. *Part. Fibre Toxicol.* **2010**, *7*, 5.
68. McClure, J.; Cameron, C. H.; Garrett, R. The Ultrastructural Features of Malakoplakia. *J. Pathol.* **1981**, *134*, 13–25.
69. Nagai, H.; Okazaki, Y.; Chew, S. H.; Misawa, N.; Yamashita, Y.; Akatsuka, S.; Ishihara, T.; Yamashita, K.; Yoshikawa, Y.; Yasui, H.; *et al.* Diameter and Rigidity of Multiwalled Carbon Nanotubes Are Critical Factors in Mesothelial Injury and Carcinogenesis. *Proc. Natl. Acad. Sci. U.S.A.* **2011**, *108*, E1330–E1338.
70. Zhang, H.; Ji, Z.; Xia, T.; Meng, H.; Low-Kam, C.; Liu, R.; Pokhrel, S.; Lin, S.; Wang, X.; Liao, Y.; *et al.* Use of Metal Oxide Nanoparticle Band Gap To Develop a Predictive Paradigm for Oxidative Stress and Acute Pulmonary Inflammation. *ACS Nano* **2012**, DOI: 10.1021/nn3010087.